ACS APPLIED ENERGY MATERIALS

www.acsaem.org Article

Electrochemical N_2 Reduction to Ammonia Using Single Au/Fe Atoms Supported on Nitrogen-Doped Porous Carbon

Sudhir K. Sahoo, Julian Heske, Markus Antonietti, Qing Qin, Martin Oschatz, and Thomas D. Kühne*

Cite This: *ACS Appl. Energy Mater.* 2020, 3, 10061−10069 Read Online

ACCESS | Metrics & More | Article Recommendations | Supporting Information

ABSTRACT: The electrochemical nitrogen reduction reaction (NRR) to ammonia (NH_3) is a promising alternative route for an NH_3 synthesis at ambient conditions to the conventional high temperature and pressure Haber−Bosch process without the need for hydrogen gas. Single metal ions or atoms are attractive candidates for the catalytic activation of non-reactive nitrogen (N_2), and for future targeted improvement of NRR catalysts, it is of utmost importance to get detailed insights into structure-performance relationships and mechanisms of N_2 activation in such structures. Here, we report density functional theory studies on the NRR catalyzed by single Au and Fe atoms supported in graphitic C_2N materials. Our results show that the metal atoms present in the structure of C_2N are the reactive sites, which catalyze the aforesaid reaction by strong adsorption and activation of N_2. We further demonstrate that a lower onset electrode potential is required for Fe−C_2N than for Au−C_2N. Thus, Fe−C_2N is theoretically predicted to be a potentially better NRR catalyst at ambient conditions than Au−C_2N owing to the larger adsorption energy of N_2 molecules. Furthermore, we have experimentally shown that single sites of Au and Fe supported on nitrogen-doped porous carbon are indeed active NRR catalysts. However, in contrast to our theoretical results, the Au-based catalyst performed slightly better with a Faradaic efficiency (FE) of 10.1% than the Fe-based catalyst with an FE of 8.4% at −0.2 V vs. RHE. The DFT calculations suggest that this difference is due to the competitive hydrogen evolution reaction and higher desorption energy of ammonia.

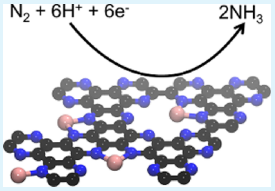

KEYWORDS: *electrochemical ammonia synthesis, nitrogen reduction reaction, single metal catalysis, nitrogen-doped carbon, density functional theory calculations*

INTRODUCTION

The synthesis of ammonia (NH_3) from nitrogen (N_2) and hydrogen (H_2) gases is a crucial chemical reaction due to its applications in fertilizers and as a carbon-free energy carrier.[1,2] Currently, NH_3 is industrially synthesized by the Haber−Bosch process using iron (Fe)-based catalysts.[3,4] The N_2 molecule, which is quite inert as evident by its large dissociation energy (~941 kJ mol^{-1}),[5] is first dissociated upon adsorption on the catalyst before reacting with H atoms in the Haber−Bosch process.[6] The dissociation of N_2 molecules requires harsh conditions, which is why NH_3 is synthesized at high temperature (400−600 °C) and high pressure (100−200 atm). Although the reaction is exothermic, high temperatures are necessary to overcome the reaction barrier, while high pressure is employed to achieve reasonable reaction rates. Moreover, endothermic steam reforming of methane, which is being used for H_2 gas supply, requires high temperature.[7] This consumes a large amount of energy (~1.5% of the world's total energy) and contributes ~2% of all greenhouse gases.[3,7] Therefore, an alternative method for the NH_3 synthesis at ambient conditions, as well as a clean and green source of H_2 gas, is highly desirable.

Electrochemical N_2 reduction, as an alternative and promising method for the NH_3 synthesis at ambient conditions, has recently gained significant attention in the scientific community.[7−24] Here, the electrochemical N_2 reduction reaction (NRR) is carried out in an electrochemical cell. Renewable electricity from solar or wind energy can be used for NH_3 production, and no H_2 gas is needed because N_2 reacts with protons and electrons, which are usually generated by electrochemical splitting of water. However, the ratio of electrons used for NH_3 production, denoted as Faradaic efficiency (FE), is still very low. The major reason for this is that the hydrogen evolution reaction (HER) competes with the NRR whenever an aqueous electrolyte is used due to the similar reaction free energies of both reactions. Therefore, an ideal NRR catalyst would increase the efficiency, as well as the selectivity for the NRR over the HER. Recently, noble metal-based catalysts for NRR were reported.[25−33] In particular, gold (Au) atoms supported on nitrogen-doped porous carbons (NDPC) as the NRR catalyst have shown to yield an FE of 12.3%.[34] Since NDPC is a porous system of chelating ligands that has "noble" character,[35] Au single sites are present in a quasi-positive oxidation state. It was suggested that the Au metal atoms present in the NDPC structure are the active sites

Received: July 24, 2020
Accepted: September 23, 2020
Published: September 23, 2020

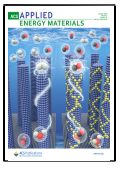

https://dx.doi.org/10.1021/acsaem.0c01740
ACS Appl. Energy Mater. 2020, 3, 10061−10069

for the NRR. The N_2 molecules adsorbed over these Au atoms are polarized due to the positive charge of Au and the negative charge of nitrogen atoms of NDPC. This frustrated Lewis pair-like structure motive is supposed to be the reason for the N−N bond activation.[34]

In this paper, we investigate the mechanism of the NRR catalyzed by single Au atoms supported in NDPC using density functional theory (DFT)-based calculations supported by experimental data. Here, the NDPC is modeled by a C_2N framework, which could be synthesized from a hexaazatriphenylene-hexacarbonitrile (HAT−CN) precursor at a lower temperature.[36] In C_2N, the uniformly distributed pores are potential sites for metal clusters or single metal atoms/ions in the supported catalyst. The nitrogenase enzyme, which fixes N_2 naturally, also contains Fe atoms.[6,8,10] Furthermore, Fe atoms have partially filled 3d orbitals that can accept the electron pairs of N_2 molecules and also can donate electrons to the antibonding molecular orbitals of N_2 molecules. Hence, the catalyst containing Fe atoms can strongly interact with N_2 molecules and can thus activate the N−N bond. In this spirit, we also investigate the mechanism of N_2 activation and conversion during the electrochemical NRR on Fe−C_2N as a catalyst.

METHODS

Computational Details. The electrochemical NRR to NH_3 is modeled by the following chemical reaction

$$N_2 + 6H^+ + 6e^- \xrightarrow{M-C_2N} 2NH_3 \quad (1)$$

where one N_2 molecule reacts with six protons (H^+) and six electrons (e^-) to form two NH_3 molecules. The free energy of formation G of different intermediates is computed by means of the computational hydrogen electrode (CHE) method proposed by Nørskov et al.[37] Using the CHE model

$$\Delta G = \Delta E - T\Delta S + \Delta E_{ZPE} + eU + \Delta G_{pH} \quad (2)$$

where ΔE is the electronic energy difference, which is computed using the DFT potential energy. Moreover, T is the temperature that is set to 300 K, whereas ΔS is the difference in entropy. For solids, the entropy S can be approximated by the vibrational entropy S_{vib} that is computed as

$$-TS_{vib} = k_BT\sum_i \ln\left\{1 - \exp\left(\frac{-h\nu_i}{k_BT}\right)\right\} - \sum_i h\nu_i\left\{\frac{1}{\exp\left(\frac{h\nu_i}{k_BT}\right) - 1}\right\} \quad (3)$$

The entropy S of the gas phase molecules was taken from the thermochemical data,[38] whereas ΔE_{ZPE} represents the difference in the zero point energy E_{ZPE}, i.e.

$$E_{ZPE} = \frac{1}{2}\sum_i h\nu_i \quad (4)$$

where h, ν_i, and k_B are Planck's constant, the frequency of the normal mode, and the Boltzmann constant, respectively. In our zero point energy and vibrational entropy calculations, the normal mode frequency for all atoms of the system was computed. The electrode potential is denoted as U and the number of electrons as e, whereas ΔG_{pH} is the correction term for pH, i.e.

$$\Delta G_{pH} = k_BT \times pH \times \ln(10) \quad (5)$$

The pH contribution is a constant shift in the free energy; hence, the value of the pH is set to zero.

The C_2N support was modeled by using a supercell ($C_{48}N_{24}$) with the lattice parameters $a = b = 16.8$ Å, $c = 13.2$ Å, $\alpha = \beta = 90.0°$, and $\gamma = 60.0°$. For the sake of simplicity, in our calculations, the C_2N model contains just one atomic layer. In order to decouple the interactions between two successive C_2N layers, a vacuum along the z-axis was added by increasing the lattice parameter to 13.2 Å. Also, at this layer separation, the adsorption energy is well-converged. The supercell contains four pores that were filled by four single neutral metal atoms.

All DFT calculations were carried out using the Vienna ab initio simulation package (VASP)[39−41] using the projector-augmented wave (PAW) method.[42] The Kohn−Sham orbitals were expanded using a plane-wave basis set with an energy cutoff of 350 eV, which is sufficient to reproduce the adsorption energy with an accuracy of 0.01 eV. The PBE exchange−correlation functional[43] together with Grimme's empirical dispersion correction[44] (PBE+D3) was employed in this work. In our DFT calculations, the explicitly treated valence orbitals are 1s for H, 2s2p for C, 2s2p for N, 3d4s for Fe, and 5d6s for Au. The first Brillouin zone was sampled using a 2 × 2 × 1 Monkhorst−Pack k-point mesh.[45] The conjugate gradient scheme was applied to optimize the structure till the ionic forces were less than 0.001 eV/Å. We have explicitly verified that there are no imaginary frequencies in all of the ground state structures investigated here.

Experimental Details. Synthesis of NDPC: As a precursor, HAT−CN was employed and carbonized at 900 °C with a heating rate of 4 °C min^{-1} for 1 h under a N_2 flow. Synthesis of gold and iron single atoms on NDPC (AuSAs−NDPC and FeSAs−NDPC): NDPC was dispersed in a mixture of water (15 mL) and ethanol (15 mL) under continuous stirring followed by adding $HAuCl_4$ aqueous solution (0.02 M) of 0.08 mL and $FeCl_3$ aqueous solution (0.02 M) of 0.2 mL. After stirring at room temperature overnight, the product was collected by centrifugation, washed with water, and dried under vacuum at 60 °C. Finally, the product was treated at 350 °C for 1 h under a flow of 5% H_2 in Ar.

The X-ray powder diffraction (XRD) patterns of the as-obtained products was measured by a Bruker D8 advance X-ray diffractometer with Cu Kα radiation. Transmission electron microscopy (TEM) and high-resolution TEM (HRTEM) studies were carried out with a double-corrected JEOL ARM 200F instrument operating at 200 kV. Our N_2 physisorption isotherms were measured on a Quadrasorb apparatus from Quantachrome Instruments at −196 °C. The samples were outgassed at 150 °C for 20 h under vacuum. UV−Vis spectroscopic measurements were conducted with a Cary 50 UV−Vis spectrometer. The electrochemical NRR was conducted with a three-electrode system using 0.1 M HCl aqueous solution as an electrolyte. Typically, the working electrode was prepared by depositing an ethanol dispersion of catalyst ink onto a carbon paper electrode, and a saturated calomel electrode (SCE) and platinum foil were used as the reference and counter electrode, respectively. All the potentials in this work were calculated with respect to a reversible hydrogen electrode (RHE), i.e.

$$E(RHE) = E(SCE) + 0.24 + 0.059pH \quad (6)$$

All the gases used have a purity of 99.999%. All the electrochemical properties were investigated on a Gamry potentiostat. The determination of NH_3 was achieved by the indophenol blue method. In detail, 2 mL of the electrolyte solution after an electrochemical test was mixed with 2 mL of a 1 M NaOH solution (contains 5 wt % sodium citrate and 5 wt % salicylic acid) followed by adding 1 mL of 0.05 M NaClO solution and 0.2 mL of 1 wt % $C_5FeN_6Na_2O$ (sodium nitroferricyanide). The as-obtained solution was measured by UV−Vis spectroscopy, and the adsorption peak of indophenol blue appeared at around 655 nm. The FE of NH_3 was calculated according to the following equation

$$FE = \frac{3FcV}{Q} \quad (7)$$

where F is the Faraday constant, c is the calculated concentration of NH_3, V is the total volume of the electrolyte within the cathodic

https://dx.doi.org/10.1021/acsaem.0c01740
ACS Appl. Energy Mater. 2020, 3, 10061−10069

compartment, and Q is the total charge passed through the electrochemical system.

RESULTS AND DISCUSSION

First, the structure of the catalyst was predicted by computing the binding energy of the isolated metal atom to the C_2N framework. In the C_2N scaffold, both C and N atoms are sp^2-hybridized, and the pyrazinic N atoms also have an electron pair, which could provide an electron donor function to the metal atom. Our results suggest that the metal forms a bond with the N atoms of the C_2N framework, as shown in Figure S1 in the Supporting Information. The binding energy per metal site is −2.40 and −6.59 eV for the Au−C_2N and Fe−C_2N catalysts, respectively. A large binding energy is indicative of a high thermodynamic stability of the catalyst and theoretically underlines the fact that the C_2N material can act as a chelating ligand leading to a strong stabilization of the metal species.

We have also computed the potential energy barrier for the diffusion of metal atoms on the surface from one of the binding sites to other equivalent positions in the C_2N framework by employing the nudged elastic band (NEB) method.[46] There are five intermediate images in our NEB calculations that were created by a linear interpolation between the end states. The force constant of the spring, which connects these intermediate images, is set to 5.0 eV $Å^{-2}$. The potential energy surfaces for the diffusion of Au and Fe atoms in Au−C_2N and Fe−C_2N are given in Figures S2 and S3 in the Supporting Information, respectively. Our results suggest that the corresponding diffusion barriers are 1.94 and 3.47 eV, respectively. The relatively high energy barrier for the diffusion of metal atoms could prevent the formation of the cluster, thus indicating the kinetic stability of the supported single atoms on the C_2N scaffold.

In the NRR, the first step is the adsorption of N_2 molecules on the catalyst. The ideal catalyst would provide strong binding sites for the N_2 molecule and thus weaken the N−N bond. Table 1 shows the free energy of adsorption of a N_2 molecule over the catalyst and the N−N bond length in the adsorbed state. Over Au−C_2N catalyst, the free energy of adsorption of N_2 is −0.14 eV, and the N−N bond length is 1.12 Å (see Figure 1a). The N_2 molecule binds more strongly over the Fe−C_2N catalyst, which entails a free energy of adsorption of −0.77 eV and a N−N bond length of 1.14 Å (see Figure 1b). In addition, the N_2 molecule can be adsorbed over Fe−C_2N in a side-wise fashion, as can be seen in Figure 1c. The corresponding free energy is −0.27 eV, and the bond length is 1.17 Å, as compared to 1.12 Å in the gas phase. Thus, the elongation of the N−N bond suggests that the N_2 molecule is activated more strongly over the Fe−C_2N catalyst. The large adsorption free energy within Fe−C_2N is most likely due to the charge transfer from the N_2 molecule to the Fe atom and vice versa (back donation). In Figure 1, the point charges of selected atoms obtained from the Bader charge analysis are given.[47] In accordance with the free energy, the point charge on the N_2 molecule over the Au−C_2N catalyst is negligible. Interestingly, however, the point charges of the N_2 molecule adsorbed over Fe−C_2N are due to the charge transfer from the catalyst. The electron density difference plot, shown in Figure 2 (also see Figure S4 of the Supporting Information), further confirms the presence of sizable charge transfer. More precisely, the electron density is accumulated on the top N atom of the N_2 molecule, as well as along the N−Fe bond, whereas the electron density is depleted along the N−N bond and from the Fe atom, as shown in Figure 2.

In the next step, we modeled the NRR catalyzed by M−C_2N. The mechanism of the NRR can in general be classified into two categories, namely, associative and dissociative mechanisms.[7,10,22] In the dissociative mechanism, the N_2 molecule adsorbed over the catalyst is first dissociated into two N atoms. These dissociated N atoms then react with three proton-electron pairs to form NH_3. By contrast, in the

Table 1. The Free Energy of Adsorption ΔG_{ads} at 300 K and Bond Length d_{N-N} of the N_2 Molecule over the M−C_2N Catalyst

catalysts	ΔG_{ads} (eV)	d_{N-N} (Å)
Au−C_2N	−0.14	1.12
Fe−C_2N	−0.77	1.14[a]
	−0.27	1.17[b]

[a]The N_2 molecule is adsorbed in an end-on fashion. [b]The N_2 molecule is adsorbed in a side-wise fashion.

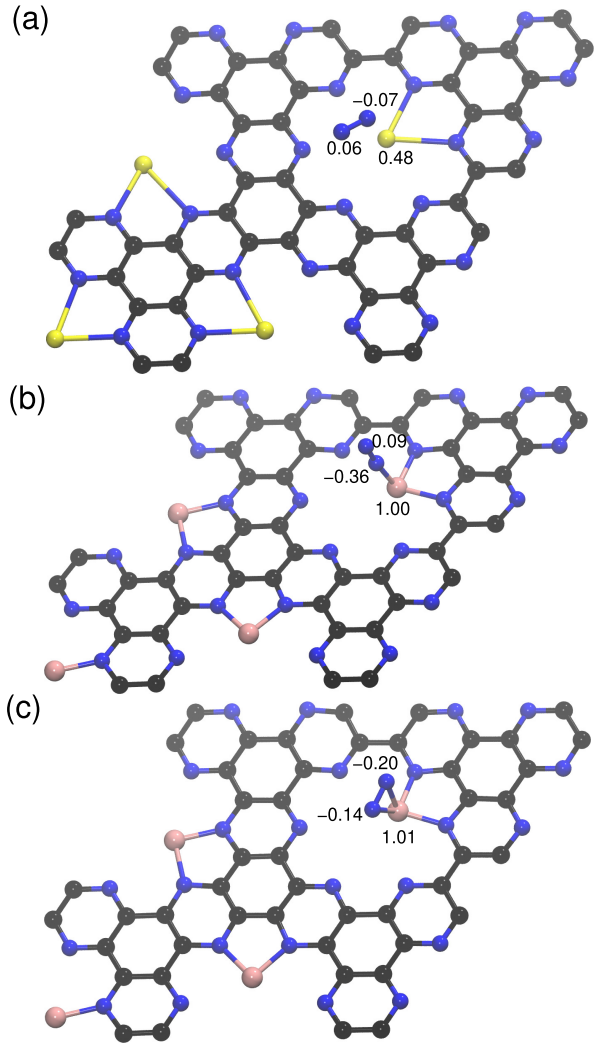

Figure 1. Atomic structure of a N_2 molecule adsorbed over Au−C_2N (a) and Fe−C_2N in an end-on (b) and side-wise (c) fashion. The partial point charges (in e unit) of the selected atoms obtained from Bader charge analysis are shown. Atom color: C−black, N−blue, Au−yellow, and Fe−pink.

https://dx.doi.org/10.1021/acsaem.0c01740
ACS Appl. Energy Mater. 2020, 3, 10061−10069

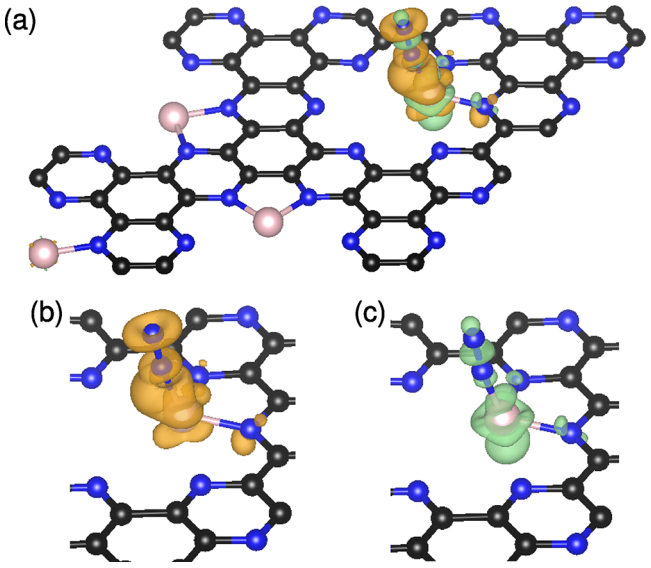

Figure 2. (a) Electron density difference (isovalue = ± 0.004 e/Å^3) plot for N_2 adsorbed over Fe−C_2N in an end-on fashion. The orange and turquoise colors represent the electron density accumulation and depletion, respectively. (b) Accumulation and (c) depletion of electron density.

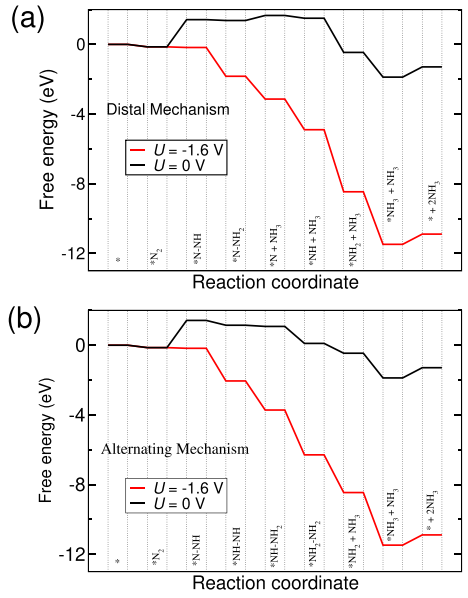

Figure 4. Free energies for the formation of the various intermediates during electrochemical N_2 reduction to NH_3 in distal (a) and alternating (b) pathways catalyzed by Au−C_2N.

associative mechanism, the N_2 molecule reacts with a proton and an electron, and the N−N bond dissociates simultaneously.[7,10,22] In both of the systems considered here, only one metal atom is present at the catalytic reaction center; thus, there is no metal site available for the dissociation of the N_2 molecule.[48] It is also reported that the dissociative adsorption of N_2 on similar systems is not thermodynamically favorable and furthermore has to overcome a high energy barrier.[49] Hence, in this study, only the associative mechanism is taken into account. The mechanism of the electrochemical reduction of N_2 to NH_3 catalyzed by similar materials has already been reported in the literature.[13,17,48−52] Three types of mechanisms are possible, namely, distal, alternating, as well as enzymatic mechanisms, as shown in Figure 3.

The corresponding free energies of formation for the various intermediates in different pathways using the Au−C_2N catalyst are given in Figure 4. Since the nature of N_2 adsorption is physisorption, only distal and alternating pathways are possible. In the distal mechanism, the distal N atom (farthest N atom from the catalyst) is hydrogenated preferentially to form NH_3, while in the alternating pathway, both of the N atoms are alternately hydrogenated.[53] Figure 4a shows the free-energy profile for the distal mechanism using the Au−C_2N catalyst, where both the formation of the *N−NH intermediate and the release of the first NH_3 molecule (*N +NH_3) are endergonic steps (Figure S5 in the Supporting Information). If a potential of −1.6 V is applied, then all single steps in this reaction pathway become exergonic. In the alternating pathway, only the first step, i.e., the formation of a *N−NH intermediate, is endergonic. The potential needed to make all steps in this mechanism exergonic is also found to be −1.6 V (see Figure 4b and Figure S6 in the Supporting Information). The desorption of a second NH_3 molecule from the catalyst, the last step of the reaction, is endergonic with a free energy of 0.59 eV.

Similarly, the electrochemical NRR to NH_3 was modeled using the Fe−C_2N catalyst. Figure 5 shows the resulting free-energy profiles in different pathways using the Fe−C_2N catalyst. In the distal pathway, the formations of *N−NH and *N−NH_2 intermediates are endergonic steps. Meanwhile, in the alternating mechanism, the formation of *NH−NH_2 is also

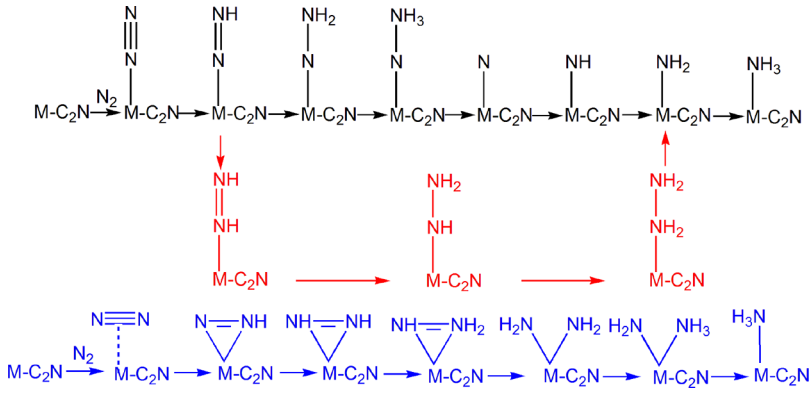

Figure 3. Schematic diagram of the electrochemical reduction of N_2 to NH_3 in distal (black), alternating (red), and enzymatic (blue) pathways. Here, M represents the metal atom supported in the C_2N framework.

https://dx.doi.org/10.1021/acsaem.0c01740
ACS Appl. Energy Mater. 2020, 3, 10061−10069

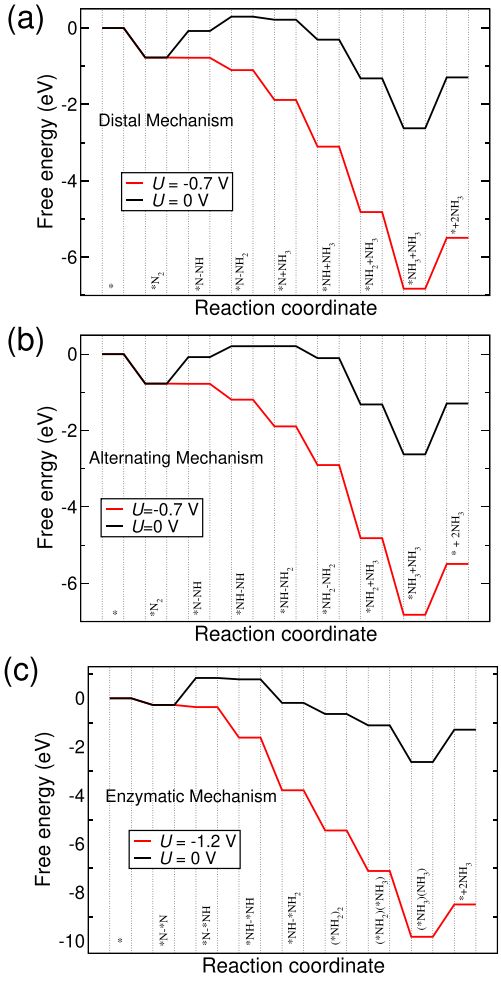

Figure 5. Free energies for the formation of the various intermediates during electrochemical N_2 reduction to NH_3 in distal (a), alternating (b), and enzymatic (c) pathways catalyzed by Fe−C_2N.

endergonic along with the formation of two other intermediates, i.e., *N−NH and *N−NH_2. Our DFT results suggest that a potential of just −0.7 V is required, such that the NRR free-energy profiles become downhill only for both the distal (Figure 5a and Figure S7 in the Supporting Information) and alternating (Figure 5b and Figure S8 in the Supporting Information) pathways. The enzymatic mechanism for the NRR is also possible in the case of this catalyst since N_2 can adsorb in a side-wise fashion. The corresponding potential necessary for the first hydrogenation to become exergonic is found to be −1.2 V for the enzymatic mechanism (see Figure 5c and Figure S9 in the Supporting Information). This potential could be ascribed to the positive free energy of formation for the *N−NH intermediate in both distal and alternating pathways and the formation of the *N−*NH intermediate in the enzymatic pathway. The necessary potential for the enzymatic pathway is found to be higher than those for both distal and alternating pathways. This is due to the N_2 adsorption energy difference since N_2 is adsorbed stronger over Fe−C_2N in an end-on fashion than the side-wise adsorption. It has been reported that the enzymatic pathway is more preferred than the distal and alternating pathways in the case of boron-doped CN-type materials such as C_3N_4 and C_2N catalysts.[50,52] However, our results suggest that the electrochemical NRR catalyzed by supported transition metal atoms on nitrogen-doped carbon proceeds via either distal or alternating mechanisms. We can now infer that the onset potential for the electrochemical NRR to NH_3 depends on the nature of the metal atoms in the C_2N-supported catalysts. Our results suggest that the onset potential for the Au−C_2N catalyst is −1.0 V higher than that for the Fe−C_2N catalyst. Moreover, this onset potential depends on the first step of hydrogenation that is the formation of a *N−NH intermediate. From this, it follows that this is the rate-determining step, which is in line with previous studies.[13,48,51,54] We ascribe this difference to the difference in N_2 adsorption energy; the N_2 molecule binds much more strongly to Fe−C_2N than to Au−C_2N.

Though the NRR mechanism can be generally classified into three types, as shown in Figure 3, in reality, however, the reaction mechanism is more complex. This is to say that instead of the complete NRR, only part of it might be continuing in a single mechanism. Hence, in order to find the most appropriate mechanism through which the NRR could be progressing, we computed the minimum free-energy pathways for Au−C_2N as well as Fe−C_2N being the catalysts. Our results suggest that with the Fe−C_2N catalyst, the NRR initially proceeds via the alternating pathway up to the formation of the *NH−NH_2 intermediate, whereas for the remaining part, the NRR proceeds through the distal pathway (Figure S10 in the Supporting Information). However, from our calculations, we also conclude that the alternating mechanism is the most favored pathway for the NRR using Au−C_2N as the catalyst.

Even though several catalysts have been proposed for the NRR, the Haber−Bosch process is still heavily used in industry. One of the main reasons for this is the low FE, which is due to the competitive HER.[10,12,14,22] Hence, in this study, we also calculated the free-energy profiles of HER using M−C_2N catalysts. The structures of *H intermediates, the H atom adsorbed on the metal atom, as obtained by our calculations, are shown in Figures S11 and S12 in the Supporting Information. Figure 6 clearly indicates that the

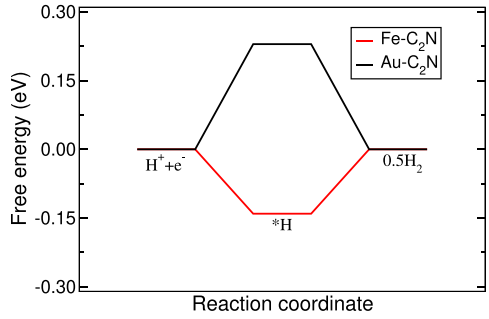

Figure 6. Free-energy profile of the HER over Au−C_2N and Fe−C_2N catalysts.

Au−C_2N catalyst is not suitable for HER due to the positive free energy of formation for the *H intermediate. However, in the case of Fe−C_2N, the formation of the *H intermediate is exergonic with a free energy of −0.14 eV. Therefore, it is expected that the HER would be competitive to NRR.

In order to investigate the role of the metal atoms in the NRR, we also investigate the NH_3 synthesis catalyzed by metal-free bare C_2N. The first step of the NRR is the adsorption of a N_2 molecule followed by the formation of a *N−NH intermediate. Our results suggest that the adsorption of N_2 is thermodynamically favorable with an adsorption

https://dx.doi.org/10.1021/acsaem.0c01740
ACS Appl. Energy Mater. 2020, 3, 10061−10069

energy of −0.18 eV, which is comparable to that of Au−C_2N. However, we find that the *N−NH intermediate, which is the second step in the NRR, is not stable in the bare C_2N scaffold but forms a *H intermediate instead as shown in Figure S13 in the Supporting Information. Thus, we can confirm that the bare C_2N scaffold is not a suitable NRR catalyst.

These theoretical calculations have been supplemented with experimental NRR data based on different catalysts. Single Fe atoms supported on NDPC (FeSAs−NDPC) are synthesized and characterized in a similar way to that of AuSAs−NDPC.[34] The XRD patterns of NDPC, AuSAs−NDPC, and FeSAs−NDPC show two broad peaks at ∼26 and ∼44°. From this, it follows that all of these materials are amorphous in nature and no larger metallic domains or nanoparticles are present, which is in line with our previous work (see Figure 7a).[34] The N_2

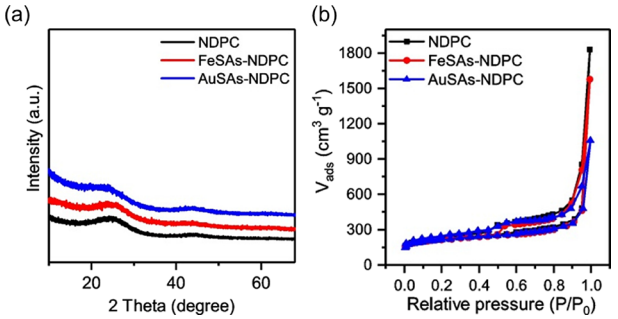

Figure 7. XRD patterns (a) and N_2 physisorption isotherms at −196 °C (b) of NDPC, FeSAs−NDPC, and AuSAs−NDPC.

physisorption isotherms of all materials confirm the presence of micropores and a very similar pore structure (Figure 7b). These micropores are potential sites for the location of single metal atoms that can act as the active centers for N_2 activation. In Figure 8, TEM images of AuSAs−NDPC further show that the material is porous with a flake-like structure. The structure of AuSAs−NDPC remains similar to that of NDPC (see Figure S14 in the Supporting Information), which indicates that the

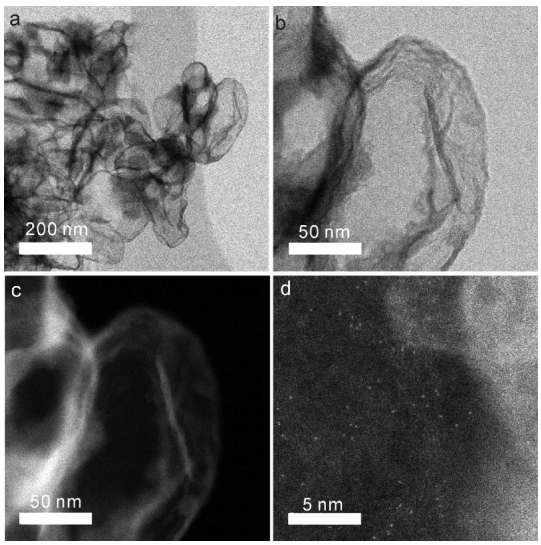

Figure 8. Representative images of AuSAs−NDPC by means of TEM (a), aberration-corrected STEM in bright-field mode (b), aberration-corrected STEM in dark-field mode (c), and high-magnification HAADF−STEM (d).

structure of the material does not change upon Au loading. Similarly, TEM images of FeSAs−NDPC confirm that the material is also porous with a flake-like structure that is very similar to that of NDPC. High-angle annular dark-field scanning TEM (HAADF−STEM) images of AuSAs−NDPC and FeSAs−NDPC indicate that isolated Au and Fe single sites (bright dots) are dispersed throughout the NDPC (Figure 7d and Figure S15d in the Supporting Information), which will eventually provide a large number of catalytic centers.

The performance of both catalysts was then experimentally verified using a two-compartment cell in a three-electrode system. For comparison, the NRR has also been carried out using NDPC as the catalyst. Table 2 shows the FE and yield of

Table 2. Comparison of the FE and NH_3 Yield for the NRR Using Metal-Supported NDPC and Bare NDPC

catalysts	Faradaic efficiency (%)	NH_3 yield ($\mu g\ cm^{-2}\ h^{-1}$)
AuSAs−NDPC	10.1	3.7
FeSAs−NDPC	8.4	2.5
NDPC	1.3	1.1

the NH_3 formation using AuSAs−NDPC, FeSAs−NDPC, and NDPC catalysts. It has been reported that at −0.2 V vs. RHE, the highest FE is achieved using AuSAs−NDPC as the NRR catalyst.[34] This is the reason why for other catalysts, the NH_3 formation is studied here at the same potential. In order to confirm that the N atoms in the NH_3 molecules originate from the N_2 gas only and in particular not from the catalyst itself, we have performed a control experiment under an Ar atmosphere.[12,55] Therein, however, no NH_3 is detected at −0.2 V vs. RHE, as shown in Figure S16 in the Supporting Information. This indicates that the N atoms in the detected NH_3 molecules are solely sourced from the N_2 gas, and it also confirms the stability of these catalysts under reaction conditions.

The catalytic performance of AuSAs−NDPC is found to be slightly higher than that of FeSAs−NDPC at −0.2 V vs. RHE, as can be seen from the corresponding FE and NH_3 yield listed in Table 2. Both materials show notable catalytic activity in NRR, which clearly confirms that the isolated metal sites are the reason for the catalytic activity. In contrast to the theoretical results, the AuSAs−NDPC has slightly better catalytic properties. This is most likely due to the competitive HER in the Fe−C_2N catalyst, as predicted by our DFT calculations (see Figure 6). Further, the desorption free energy of the NH_3 molecule for the Fe−C_2N catalyst is higher than that on Au−C_2N. Our results suggest that an energy of 1.33 eV is required to desorb the NH_3 molecule from the Fe−C_2N catalyst, whereas only 0.59 eV is required in the case of Au−C_2N as the catalyst. Moreover, the C_2N-type structure used within our DFT calculations is an idealized model of NDPC, whereas the experimentally applied nitrogen-doped carbon supports have lower nitrogen content and a more disordered structure. The interactions between isolated metal sites and the disordered nitrogen-doped carbon support might be affecting the N_2 activation, which is eventually the reason for the superior catalytic performance in AuSAs−NDPC. In accordance with the present theoretical investigations, a very low FE of 1.3% and an NH_3 yield of 1.1 $\mu g\ cm^{-2}\ h^{-1}$ is detected when bare NDPC is used as the catalyst.

https://dx.doi.org/10.1021/acsaem.0c01740
ACS Appl. Energy Mater. 2020, 3, 10061−10069

CONCLUSIONS

We have employed DFT-based calculations to elucidate the underlying mechanism of the electrochemical NRR to NH_3 catalyzed by single Au and Fe atoms supported in a layered C_2N material. From our results, we conclude that the metal atoms (Fe and Au), which are present in the pore and bonded to the N atoms of the C_2N framework, are the active sites for the reaction. Furthermore, in the Fe−C_2N catalyst, both distal and alternating pathways are preferred over the enzymatic pathway. The onset potential is only −0.7 V for both distal and alternating pathways, whereas it is −1.2 V for the enzymatic pathway. The observed onset potential is due to the formation of a *N−NH intermediate that is thus the rate-determining step in the NRR. Similarly, for the Au−C_2N catalyst, the onset potential is found to be −1.6 V, which is higher than that for the Fe−C_2N catalyst. Hence, it is computationally predicted that Fe−C_2N is potentially a better catalyst than Au−C_2N owing to the lower onset potential of the former. We have also experimentally demonstrated that single Au/Fe sites supported in C_2N−like NDPC are active NRR catalysts, which is in agreement with the present theoretical prediction. However, in contrast to the latter, the usage of an Au-based catalyst is still slightly superior to the here suggested Fe-based one. Our DFT results suggest that this is due to the competitive HER and higher desorption energy of ammonia molecules in Fe-based catalysts.

ASSOCIATED CONTENT

Supporting Information

The Supporting Information is available free of charge at https://pubs.acs.org/doi/10.1021/acsaem.0c01740.

Atomic structures of Au−C_2N and Fe−C_2N, potential energy surfaces for the diffusion of Au and Fe atoms on the C_2N surface, zero point energy, vibrational entropy and atomic structures of various intermediates, TEM images of NDPC and Fe−NDPC, and convergence of adsorption energy with respect to plane-wave energy cutoff and vacuum distance (PDF)

AUTHOR INFORMATION

Corresponding Author

Thomas D. Kühne − *Dynamics of Condensed Mater and Center for Sustainable System Design, Chair of Theoretical Chemistry and Paderborn Center for Parallel Computing and Institute for Lightweight Design, University of Paderborn, Paderborn D-33098, Germany*; Email: tdkuehne@mail.uni-paderborn.de

Authors

Sudhir K. Sahoo − *Dynamics of Condensed Mater and Center for Sustainable System Design, Chair of Theoretical Chemistry, University of Paderborn, Paderborn D-33098, Germany*; orcid.org/0000-0002-3040-4466

Julian Heske − *Dynamics of Condensed Mater and Center for Sustainable System Design, Chair of Theoretical Chemistry, University of Paderborn, Paderborn D-33098, Germany; Department of Colloid Chemistry, Max Planck Institute of Colloids and Interfaces, Potsdam D-14476, Germany*

Markus Antonietti − *Department of Colloid Chemistry, Max Planck Institute of Colloids and Interfaces, Potsdam D-14476, Germany*; orcid.org/0000-0002-8395-7558

Qing Qin − *Department of Colloid Chemistry, Max Planck Institute of Colloids and Interfaces, Potsdam D-14476, Germany*; orcid.org/0000-0001-5632-1100

Martin Oschatz − *Department of Colloid Chemistry, Max Planck Institute of Colloids and Interfaces, Potsdam D-14476, Germany*; orcid.org/0000-0003-2377-1214

Complete contact information is available at: https://pubs.acs.org/10.1021/acsaem.0c01740

Notes

The authors declare no competing financial interest.

ACKNOWLEDGMENTS

This project has received funding from the European Research Council (ERC) under the European Union's Horizon 2020 Research and Innovation Programme (grant agreement no. 716142). Part of this work was funded by the Deutsche Forschungsgemeinschaft (DFG, German Research Foundation) under Germany's Excellence Strategy—EXC 2008/1 (UniSysCat)—390540038. The authors gratefully acknowledge the Gauss Centre for Supercomputing e.V. (www.gauss-centre.eu) for funding this project (application no. 13178) by providing computing time through the John von Neumann Institute for Computing (NIC) on the GCS Supercomputer JUWELS at Jülich Supercomputing Centre (JSC). The generous allocation of computing time by the Paderborn Center for Parallel Computing (PC^2) on OCuLUS and the FPGA-based supercomputer NOCTUA is kindly acknowledged.

REFERENCES

(1) Erisman, J. W.; Sutton, M. A.; Galloway, J.; Klimont, Z.; Winiwarter, W. How a century of ammonia synthesis changed the world. *Nat. Geosci.* **2008**, *1*, 636−639.

(2) Schlögl, R. Catalytic Synthesis of Ammonia-A "Never-Ending Story"? *Angew. Chem., Int. Ed.* **2003**, *42*, 2004−2008.

(3) Wang, L.; Xia, M.; Wang, H.; Huang, K.; Qian, C.; Maravelias, C. T.; Ozin, G. A. Greening Ammonia toward the Solar Ammonia Refinery. *Joule* **2018**, *2*, 1055−1074.

(4) Licht, S.; Cui, B.; Wang, B.; Li, F.-F.; Lau, J.; Liu, S. Ammonia synthesis by N_2 and steam electrolysis in molten hydroxide suspensions of nanoscale Fe_2O_3. *Science* **2014**, *345*, 637−640.

(5) Shilov, A. E. Catalytic reduction of molecular nitrogen in solutions. *Russ. Chem. Bull.* **2003**, *52*, 2555−2562.

(6) Jia, H.-P.; Quadrelli, E. A. Mechanistic aspects of dinitrogen cleavage and hydrogenation to produce ammonia in catalysis and organometallic chemistry: relevance of metal hydride bonds and dihydrogen. *Chem. Soc. Rev.* **2014**, *43*, 547−564.

(7) Li, M.; Huang, H.; Low, J.; Gao, C.; Long, R.; Xiong, Y. Recent Progress on Electrocatalyst and Photocatalyst Design for Nitrogen Reduction. *Small Methods* **2019**, *3*, 1800388.

(8) van der Ham, C. J. M.; Koper, M. T. M.; Hetterscheid, D. G. H. Challenges in reduction of dinitrogen by proton and electron transfer. *Chem. Soc. Rev.* **2014**, *43*, 5183−5191.

(9) Cui, X.; Tang, C.; Zhang, Q. A Review of Electrocatalytic Reduction of Dinitrogen to Ammonia under Ambient Conditions. *Adv. Energy Mater.* **2018**, *8*, 1800369.

(10) Liu, H.; Wei, L.; Liu, F.; Pei, Z.; Shi, J.; Wang, Z.-j.; He, D.; Chen, Y. Homogeneous, Heterogeneous, and Biological Catalysts for Electrochemical N_2 Reduction toward NH_3 under Ambient Conditions. *ACS Catal.* **2019**, *9*, 5245−5267.

(11) McPherson, I. J.; Sudmeier, T.; Fellowes, J.; Tsang, S. C. E. Materials for electrochemical ammonia synthesis. *Dalton Trans.* **2019**, *48*, 1562−1568.

(12) Suryanto, B. H. R.; Du, H.-L.; Wang, D.; Chen, J.; Simonov, A. N.; MacFarlane, D. R. Challenges and prospects in the catalysis of electroreduction of nitrogen to ammonia. *Nat. Catal.* **2019**, *2*, 290−296.
(13) Guo, C.; Ran, J.; Vasileff, A.; Qiao, S.-Z. Rational design of electrocatalysts and photo(electro)catalysts for nitrogen reduction to ammonia (NH_3) under ambient conditions. *Energy Environ. Sci.* **2018**, *11*, 45−56.
(14) Liu, X.; Jiao, Y.; Zheng, Y.; Jaroniec, M.; Qiao, S.-Z. Building Up a Picture of the Electrocatalytic Nitrogen Reduction Activity of Transition Metal Single-Atom Catalysts. *J. Am. Chem. Soc.* **2019**, *141*, 9664−9672.
(15) Ling, C.; Ouyang, Y.; Li, Q.; Bai, X.; Mao, X.; Du, A.; Wang, J. A General TwoStep Strategy−Based High-Throughput Screening of Single Atom Catalysts for Nitrogen Fixation. *Small Methods* **2019**, *3*, 1800376.
(16) Choi, C.; Back, S.; Kim, N.-Y.; Lim, J.; Kim, Y.-H.; Jung, Y. Suppression of Hydrogen Evolution Reaction in Electrochemical N_2 Reduction Using Single-Atom Catalysts: A Computational Guideline. *ACS Catal.* **2018**, *8*, 7517−7525.
(17) Zhang, X.; Chen, A.; Zhang, Z.; Zhou, Z. Double-atom catalysts: transition metal dimer-anchored C_2N monolayers as N_2 fixation electrocatalysts. *J. Mater. Chem. A* **2018**, *6*, 18599−18604.
(18) Gao, Y.; Cao, Y.; Zhuo, H.; Sun, X.; Gu, Y.; Zhuang, G.; Deng, S.; Zhong, X.; Wei, Z.; Li, X.; Wang, J.-g. Mo_2TiC_2 MXene: A Promising Catalyst for Electrocatalytic Ammonia Synthesis. *Catal. Today* **2020**, *339*, 120−126.
(19) Wang, M.; Liu, S.; Qian, T.; Liu, J.; Zhou, J.; Ji, H.; Xiong, J.; Zhong, J.; Yan, C. Over 56.55% Faradaic efficiency of ambient ammonia synthesis enabled by positively shifting the reaction potential. *Nat. Commun.* **2019**, *10*, 341.
(20) Shipman, M. A.; Symes, M. D. Recent progress towards the electrosynthesis of ammonia from sustainable resources. *Catal. Today* **2017**, *286*, 57−68.
(21) Wang, J.; Chen, S.; Li, Z.; Li, G.; Liu, X. Recent Advances in Electrochemical Synthesis of Ammonia through Nitrogen Reduction under Ambient Conditions. *ChemElectroChem* **2020**, *7*, 1067−1079.
(22) Wen, X.; Guan, J. Recent advancement in the electrocatalytic synthesis of ammonia. *Nanoscale* **2020**, *12*, 8065−8094.
(23) Lü, F.; Zhao, S.; Guo, R.; He, J.; Peng, X.; Bao, H.; Fu, J.; Han, L.; Qi, G.; Luo, J.; Tang, X.; Liu, X. Nitrogen-coordinated single Fe sites for efficient electrocatalytic N_2 fixation in neutral media. *Nano Energy* **2019**, *61*, 420−427.
(24) John, J.; Lee, D.-K.; Sim, U. Photocatalytic and electrocatalytic approaches towards atmospheric nitrogen reduction to ammonia under ambient conditions. *Nano Convergence* **2019**, *6*, 15.
(25) Suryanto, B. H. R.; Wang, D.; Azofra, L. M.; Harb, M.; Cavallo, L.; Jalili, R.; Mitchell, D. R. G.; Chatti, M.; MacFarlane, D. R. MoS_2 Polymorphic Engineering Enhances Selectivity in the Electrochemical Reduction of Nitrogen to Ammonia. *ACS Energy Lett.* **2019**, *4*, 430−435.
(26) Yao, Y.; Wang, H.; Yuan, X.-z.; Li, H.; Shao, M. Electrochemical Nitrogen Reduction Reaction on Ruthenium. *ACS Energy Lett.* **2019**, *4*, 1336−1341.
(27) Nazemi, M.; El-Sayed, M. A. The Role of Oxidation of Silver in Bimetallic Gold−Silver Nanocages on Electrocatalytic Activity of Nitrogen Reduction Reaction. *J. Phys. Chem. C* **2019**, *123*, 11422−11427.
(28) Liu, H.-M.; Han, S.-H.; Zhao, Y.; Zhu, Y.-Y.; Tian, X.-L.; Zeng, J.-H.; Jiang, J.-X.; Xia, B. Y.; Chen, Y. Surfactant-free atomically ultrathin rhodium nanosheet nanoassemblies for efficient nitrogen electroreduction. *J. Mater. Chem. A* **2018**, *6*, 3211−3217.
(29) Huang, H.; Xia, L.; Shi, X.; Asiri, A. M.; Sun, X. Ag nanosheets for efficient electrocatalytic N_2 fixation to NH_3 under ambient conditions. *Chem. Commun.* **2018**, *54*, 11427−11430.
(30) Shi, M.-M.; Bao, D.; Wulan, B.-R.; Li, Y.-H.; Zhang, Y.-F.; Yan, J.-M.; Jiang, Q. Au Sub-Nanoclusters on TiO_2 toward Highly Efficient and Selective Electrocatalyst for N_2 Conversion to NH3 at Ambient Conditions. *Adv. Mater.* **2017**, *29*, 1606550.
(31) Bao, D.; Zhang, Q.; Meng, F.-L.; Zhong, H.-X.; Shi, M.-M.; Zhang, Y.; Yan, J.-M.; Jiang, Q.; Zhang, X.-B. Electrochemical Reduction of N_2 under Ambient Conditions for Artificial N_2 Fixation and Renewable Energy Storage Using N_2/NH_3 Cycle. *Adv. Mater.* **2017**, *29*, 1604799.
(32) Wang, X.; Wang, W.; Qiao, M.; Wu, G.; Chen, W.; Yuan, T.; Xu, Q.; Chen, M.; Zhang, Y.; Wang, X.; Wang, J.; Ge, J.; Hong, X.; Li, Y.; Wu, Y.; Li, Y. Atomically dispersed Au1 catalyst towards efficient electrochemical synthesis of ammonia. *Sci. Bull.* **2018**, *63*, 1246−1253.
(33) Tan, L.; Yang, N.; Huang, X.; Peng, L.; Tong, C.; Deng, M.; Tang, X.; Li, L.; Liao, Q.; Wei, Z. Synthesis of ammonia via electrochemical nitrogen reduction on high-index faceted Au nanoparticles with a high faradaic efficiency. *Chem. Commun.* **2019**, *55*, 14482−14485.
(34) Qin, Q.; Heil, T.; Antonietti, M.; Oschatz, M. Single-Site Gold Catalysts on Hierarchical N-Doped Porous Noble Carbon for Enhanced Electrochemical Reduction of Nitrogen. *Small Methods* **2018**, *2*, 1800202.
(35) Antonietti, M.; Oschatz, M. The Concept of "Noble, Heteroatom-Doped Carbons," Their Directed Synthesis by Electronic Band Control of Carbonization, and Applications in Catalysis and Energy Materials. *Adv. Mater.* **2018**, *30*, 1706836.
(36) Walczak, R.; Kurpil, B.; Savateev, A.; Heil, T.; Schmidt, J.; Qin, Q.; Antonietti, M.; Oschatz, M. Template- and Metal-Free Synthesis of Nitrogen-Rich Nanoporous "Noble" Carbon Materials by Direct Pyrolysis of a Preorganized Hexaazatriphenylene Precursor. *Angew. Chem., Int. Ed.* **2018**, *57*, 10765−10770.
(37) Nørskov, J. K.; Rossmeisl, J.; Logadottir, A.; Lindqvist, L.; Kitchin, J. R.; Bligaard, T.; Jónsson, H. Origin of the Overpotential for Oxygen Reduction at a Fuel-Cell Cathode. *J. Phys. Chem. B* **2004**, *108*, 17886−17892.
(38) Chase, M. W. *NIST-JANAF Thermochemical Tables*. J. Phys. Chem. Ref. Data. 1998
(39) Kresse, G.; Joubert, D. From ultrasoft pseudopotentials to the projector augmentedwave method. *Phys. Rev. B* **1999**, *59*, 1758−1775.
(40) Kresse, G.; Furthmüller, J. Efficient iterative schemes for ab initio total-energy calculations using a plane-wave basis set. *Phys. Rev. B* **1996**, *54*, 11169−11186.
(41) Kresse, G.; Furthmüller, J. Efficiency of ab-initio total energy calculations for metals and semiconductors using a plane-wave basis set. *Comput. Mater. Sci.* **1996**, *6*, 15−50.
(42) Blöchl, P. E. Projector augmented-wave method. *Phys. Rev. B* **1994**, *50*, 17953−17979.
(43) Perdew, J. P.; Burke, K.; Ernzerhof, M. Generalized Gradient Approximation Made Simple. *Phys. Rev. Lett.* **1996**, *77*, 3865−3868.
(44) Grimme, S.; Antony, J.; Ehrlich, S.; Krieg, H. A consistent and accurate *ab initio* parametrization of density functional dispersion correction (DFT-D) for the 94 elements H-Pu. *J. Chem. Phys.* **2010**, *132*, 154104.
(45) Monkhorst, H. J.; Pack, J. D. Special points for Brillouin-zone integrations. *Phys. Rev. B* **1976**, *13*, 5188−5192.
(46) Henkelman, G.; Jónsson, H. Improved tangent estimate in the nudged elastic band method for finding minimum energy paths and saddle points. *J. Chem. Phys.* **2000**, *113*, 9978−9985.
(47) Henkelman, G.; Arnaldsson, A.; Jónsson, H. A fast and robust algorithm for Bader decomposition of charge density. *Comput. Mater. Sci.* **2006**, *36*, 354−360.
(48) Chen, Z.; Zhao, J.; Cabrera, C. R.; Chen, Z. Computational Screening of Efficient Single-Atom Catalysts Based on Graphitic Carbon Nitride ($g\text{-}C_3N_4$) for Nitrogen Electroreduction. *Small Methods* **2019**, *3*, 1800368.
(49) Wang, Z.; Yu, Z.; Zhao, J. Computational screening of a single transition metal atom supported on the C_2N monolayer for electrochemical ammonia synthesis. *Phys. Chem. Chem. Phys.* **2018**, *20*, 12835−12844.
(50) Ling, C.; Niu, X.; Li, Q.; Du, A.; Wang, J. Metal-Free Single Atom Catalyst for N_2 Fixation Driven by Visible Light. *J. Am. Chem. Soc.* **2018**, *140*, 14161−14168.

https://dx.doi.org/10.1021/acsaem.0c01740
ACS Appl. Energy Mater. 2020, 3, 10061−10069

(51) Chen, Z. W.; Yan, J.-M.; Jiang, Q. Single or Double: Which Is the Altar of Atomic Catalysts for Nitrogen Reduction Reaction? *Small Methods* **2019**, *3*, 1800291.
(52) Ji, S.; Wang, Z.; Zhao, J. A boron-interstitial doped C_2N layer as a metal-free electrocatalyst for N_2 fixation: a computational study. *J. Mater. Chem. A* **2019**, *7*, 2392−2399.
(53) Guo, X.; Du, H.; Qu, F.; Li, J. Recent progress in electrocatalytic nitrogen reduction. *J. Mater. Chem. A* **2019**, *7*, 3531−3543.
(54) Skúlason, E.; Bligaard, T.; Gudmundsdóttir, S.; Studt, F.; Rossmeisl, J.; Abild-Pedersen, F.; Vegge, T.; Jónsson, H.; Nørskov, J. K. A theoretical evaluation of possible transition metal electro-catalysts for N_2 reduction. *Phys. Chem. Chem. Phys.* **2012**, *14*, 1235−1245.
(55) Li, L.; Tang, C.; Yao, D.; Zheng, Y.; Qiao, S.-Z. Electrochemical Nitrogen Reduction: Identification and Elimination of Contamination in Electrolyte. *ACS Energy Lett.* **2019**, *4*, 2111−2116.

https://dx.doi.org/10.1021/acsaem.0c01740
ACS Appl. Energy Mater. 2020, 3, 10061−10069